frontiers | Frontiers in Astronomy and Space Sciences

TYPE Original Research
PUBLISHED 25 May 2023
DOI 10.3389/fspas.2023.1179558

OPEN ACCESS

EDITED BY
Josep M. Trigo-Rodríguez,
Spanish National Research Council (CSIC), Spain

REVIEWED BY
Akos Kereszturi,
Hungarian Academy of Sciences (MTA), Hungary
Jianguo Yan,
Wuhan University, China

*CORRESPONDENCE
Guangfei Wei,
gfwei0554@gmail.com
Hong Gan,
ganhong06@gmail.com

RECEIVED 04 March 2023
ACCEPTED 12 May 2023
PUBLISHED 25 May 2023

CITATION
Wei G, Li X, Gan H and Shi Y (2023), Retrieval of lunar polar heat flow from Chang'E-2 microwave radiometer and Diviner observations.
Front. Astron. Space Sci. 10:1179558.
doi: 10.3389/fspas.2023.1179558

Retrieval of lunar polar heat flow from Chang'E-2 microwave radiometer and Diviner observations

Guangfei Wei[1,2]*, Xiongyao Li[2,3], Hong Gan[1]* and Yaolin Shi[4]

[1]Deep Space Exploration Laboratory, Hefei, China, [2]Center for Excellence in Comparative Planetology, Chinese Academy of Sciences (CAS), Hefei, China, [3]Center for Lunar and Planetary Sciences, Institute of Geochemistry CAS, Guiyang, China, [4]Key Laboratory of Computational Geodynamics, College of Earth and Planetary Sciences, University of Chinese Academy of Sciences, Beijing, China

The internal heat flow related to the Moon's composition, interior structure, and evolution history is not well-constrained and understood on a global scale. Up to now, only two *in situ* heat flow experiments, Apollo 15 and 17 were deployed nearly 50 years ago. The measured high values of heat flow might be influenced by lateral heat at highland/mare boundaries and enhanced by heat production from radioactive elements enriched unit, and may also be disturbed by astronauts' activities. In this study, we proposed a new method to retrieve heat flows at two permanently shadowed craters, Haworth and Shoemaker of the Moon's south pole, from Chang'E-2 microwave radiometer data and Diviner observations. Our results show that the average heat flow is 4.9 ± 0.2 mW/m^2. This provides a constraint for the bulk concentration of Thorium within the lunar south polar crust 656 ± 54 ppb, which helps us understand the Moon's thermal evolution and differentiation.

KEYWORDS

Chang'E-2, microwave radiometer, Diviner, Moon, pole, heat flow, thermal model

1 Introduction

The interior heat flow provides a direct method for constraining the bulk abundance of radiogenic elements (e.g., U, Th, and K) which helps us to understand the differentiation and thermal history of the Moon (Langseth et al., 1976; Warren and Rasmussen, 1987; Wieczorek and Phillips, 2000; Siegler and Smrekar, 2014). The accurate interpretation of internal heat flow is also important to understand the volcanic history of the Moon such as the occurrence of moderately fresh "Irregular Mare Patches" (Qiao et al., 2021). Nearly 50 years ago, only two *in situ* heat flow experiments (HFEs) at the Hadley Rille and Taurus-Littrow during Apollo 15 and 17 missions obtained values of 21 ± 3 and 14 ± 2 mW/m^2, respectively (Langseth et al., 1976). However, the radiogenic elements enriched unit, Procellarum potassium, rare earth element, and phosphorus (KREEP) Terrane (PKT) (Jolliff et al., 2000), which extends to Apollo 15 landing site that likely contributes 5 ± 2 mW/m^2 to the heat flow value (Wieczorek and Phillips, 2000) and even might affect Apollo 17 heat flow measurement (Siegler and Smrekar, 2014). In addition, the two landing sites located at the boundary between the highlands and maria could also cause an additional 15%–20% heat flow (Warren and Rasmussen, 1987) and the uncertainty of the regolith thermal conductivity (Grott et al., 2010). It is worth noting that astronaut-induced surface regolith disturbance may also lead to an increase in its temperature due to the darkened surface in addition to

altering the regolith texture and surface photometric properties (Nagihara et al., 2018). This might need 5–7 years to reach the equilibrium state (Langseth et al., 1976).

Langseth et al. (1976) estimated the global average heat flow value as 18 ± 2 mW/m^2 based on Th concentration, but they still cautioned that further data should be obtained to estimate the global average value. Warren and Rasmussen (1987) considered the effects of insulation of mega regolith on lunar thermal evolution and revised the global average value to 12 ± 2 mW/m^2. Nevertheless, some researchers proposed that the measured Apollo heat flows might not be representative which overestimates the global average heat flow by up to a factor of 3 due to thermal pathways and heat-producing material of the top ~100 km of the Moon (Warren and Rasmussen, 1987; Wieczorek and Phillips, 2000; Hagermann and Tanaka, 2006; Saito, 2008). Therefore, it has been concluded that the current heat flow data is not enough to constrain the thermal state of the Moon with a 100% confidence (Hagermann and Tanaka, 2006), and the limited location of Apollo HFEs emphasizes the importance of additional, geophysical different observations to better constrain the Moon's heat flow, which has been recognized as a high priority lunar science objective (Kiefer, 2012).

After Apollo, planetary heat flow mapping was focused on the potential of orbiting microwave radiometer experiments (Keihm and Langseth, 1975; Schloerb et al., 1976; Keihm, 1984; Siegler and Smrekar, 2014). Some efforts of spectral gradients and regolith physical properties are combined to interpret ground-based microwave observations for deriving heat flow (Keihm and Langseth, 1975), which unfortunately, no orbital exploration mission has been reported as of yet. Since the long-term subsurface temperature drift of Apollo HFEs was thought to stem from the astronaut activity (Langseth et al., 1976), the regolith-uninterrupted orbital microwave observations have the advantage and capability to extend the HFE to a global scale remotely. Because the temperature in the upper 1.5 m of the sunlit regolith is strongly affected by the diurnal or annual thermal waves (Kiefer, 2012), permanently shadowed regions (PSRs) of lunar poles are supposed to be ideal places to map lunar heat flow from orbit (Paige et al., 2010; Paige and Siegler, 2016). Since there is no direct solar heat perturbation within PSRs (but could be warmed up by reflected sunlight and thermal infrared radiation from surrounding crater walls), the heat flow plays an important role in the near-surface temperature (Paige et al., 2010; Paige and Siegler, 2016). This can be sensed by microwave observations which help us to characterize the lunar near-surface thermal environment and retrieve interior heat flow. Additionally, because of the large penetration depth of microwaves, the plausible buried water ice at PSRs could also be revealed by subsurface thermal regime measurements (Meng et al., 2010), which provides landing site selection for future polar missions (e.g., De Rosa et al., 2012; Wei et al., 2023).

In this study, we propose a new method to combine the Diviner and Chang'E-2 (CE-2) microwave data to retrieve heat flow at PSRs of the Moon's south pole. In Section 2, we first use nearly 10 years (from 5 July 2009, to 17 Feb 2019) of the Diviner measurements (Paige et al., 2010; Elder et al., 2019) as surface temperature constraints to improve the thermal model. Then we model microwave emission with different heat flows to match CE-2's Microwave Radiometer (MRM) observations (Zheng et al., 2019). Lastly, we can search for the best heat flow value from different

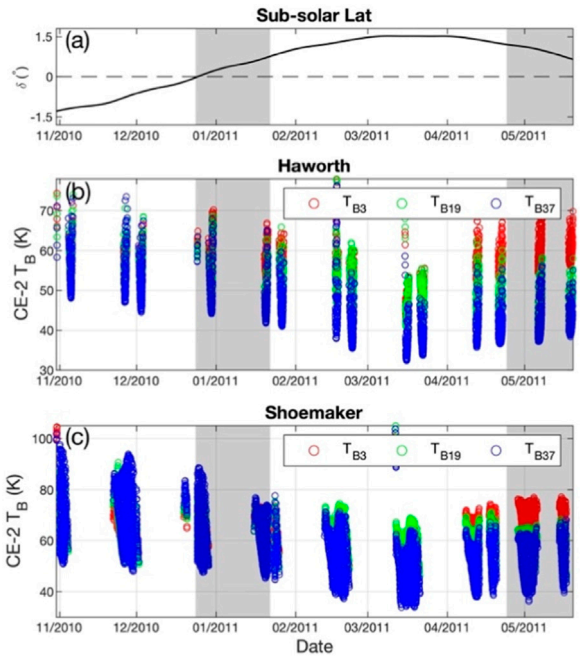

FIGURE 1
Seasonal variations of CE-2 observations at permanently shadowed craters of the Moon's south pole. **(A)** is the variation of the sub-solar latitude during the CE-2 mission. The dashed line denotes the equator. **(B)** and **(C)** are variations of T_{B3}, T_{B19} and T_{B37} near the bottom of Haworth and Shoemaker, respectively. The time span covered by gray areas indicates the observations used in this study.

MRM channels' data. In Section 3, we present the retrieved heat flow at two permanently shadowed craters. A detailed discussion of possible factors that influence our inversion results is presented in Section 4 and a conclusion is followed in Section 5.

2 Dataset and methodology

2.1 Chang'E-2 microwave radiometer data

Microwave Radiometer onboard CE-2 measured lunar surface with four channels $(c_i, i = 1, 2, 3, 4)$, i.e., 3, 7.8, 19.35 and 37 GHz, in a polar orbit at an altitude of ~100 km (Zheng et al., 2019). Channel 1 observed the lunar surface with a spatial resolution of 25 km and the others with 17.5 km. More details about MRM have been introduced in Zheng et al. (2019). Figure 1A shows the variation of sub-solar latitude (δ) during the CE-2 mission, which covers part of the southern summer ($\delta < 0$) and most of the southern winter ($\delta > 0$). Figures 1B, C shows seasonal fluctuations of CE-2's MRM observations at 3 (T_{B3}), 19.35 (T_{B19}), and 37 GHz (T_{B37}) near the bottom of Haworth and Shoemaker craters. It can be seen that the MRM observation behaves as a seasonal variation during the mission, which has good agreement with the Diviner measurements (Williams et al., 2019). This seasonal effect is caused by the scattered sunlight and infrared radiation from ambient crater walls. The different amplitude of T_B at the same frequency between Haworth and Shoemaker also indicates different

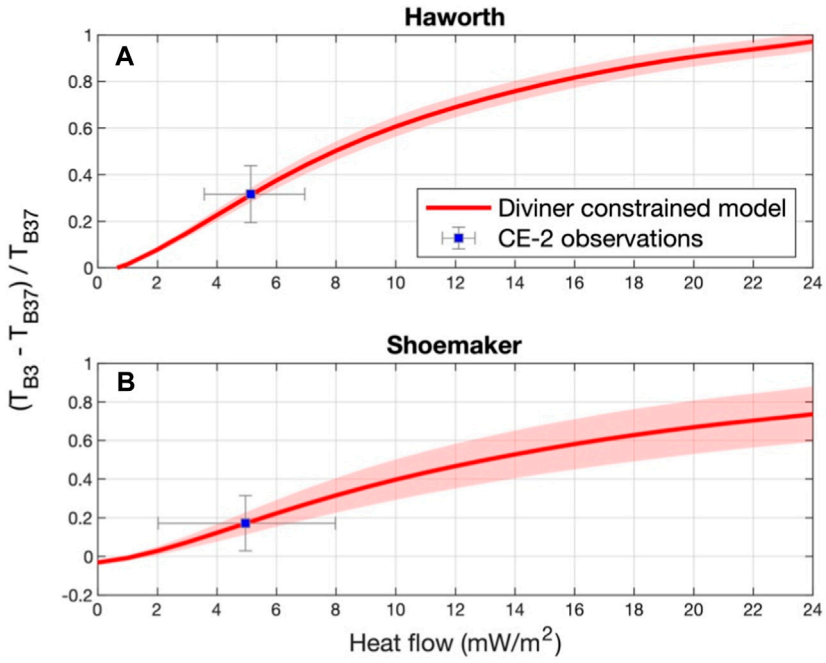

FIGURE 2
Comparison of $r_{1,4} = (c_1 - c_4)/c_4$ between CE-2 observations and Diviner constrained model at **(A)** Haworth and **(B)** Shoemaker. The vertical bar of CE-2 observations is the standard deviation, and the horizontal bar is the corresponding heat flow range. The red-shaded area is the standard deviation of modeled values.

thermal environments, thermophysical properties of regolith, and possible heat flow.

Considering the relatively small seasonal effect and more MRM data coverage during southern winter, both Diviner and MRM data obtained within this season are selected. Although the MRM observations present an apparent seasonal variation, the potential calibration issues due to CE-2 reorientation on the cold horn (a set of calibration antennas pointing to cold space for reference) for terminator orbits (Feng et al., 2020) between 22 Jan 2011, and 24 April 2011, were excluded. Thus, the data points near the bottom of Haworth and Shoemaker during southern winter are selected which are shown in the gray areas of Figure 1.

2.2 Diviner data

The Diviner Lunar Radiometer (Diviner (Paige et al., 2010)) onboard the Lunar Reconnaissance Orbiter systematically maps lunar surface thermal environment for more than 10 years since July 2009 (Williams et al., 2019). Diviner including 9 channels was designed to measure reflected solar radiation (each of the first two channels 0.35–2.8 μm) and infrared emission (other seven channels range from 7.55 to 400 μm) with a spatial resolution of ~200 m globally (Paige et al., 2010). Recently, the bolometric brightness temperature (T_{bol}) covering polar regions generated from nearly 10 years of Diviner measurements have been compiled into diurnal temperatures at southern summer/winter according to the variation of sub-solar latitudes (Williams et al., 2019). In our study, the T_{bol} data within southern winter corresponding to CE-2 observations were used as surface thermal constraints for the thermal model. And the southern summer T_{bol} data were used to investigate the maximum seasonal effect on the thermal stability of water ice in the lunar south polar region.

2.3 Improved thermal model

We use the one-dimensional thermal model to calculate the lunar polar subsurface temperatures (Vasavada, 1999; Paige et al., 2010; Vasavada et al., 2012; Hayne et al., 2017).

$$\rho(z)C(T)\frac{\partial T}{\partial t} = \frac{\partial}{\partial z}\left[K(T,z)\frac{\partial T}{\partial z}\right] \quad (1)$$

where T is the temperature, z is the depth, $\rho(z)$ is the bulk density which is dependent upon depth, $C(T)$ is the specific heat capacity which is a function of temperature, and $K(T,z)$ is the thermal conductivity of lunar regolith which depends on both temperature and depth. Vasavada et al. (2012) proposed to use the H parameter in an exponential form to characterize bulk density and thermal conductivity based on Diviner measurements; Hayne et al. (2017) derived the global distribution of the H parameter based on Vasavada et al.'s model and rock-free regolith temperature (Bandfield et al., 2011). The global mean H value 0.07 m was adopted in this study to characterize the density profile of the soil. Note that the thermophysical property of soils at extremely low temperatures (as low as 20 K) becomes complex which is a lack of comprehensive laboratory measurements. Recently, Woods-Robinson et al., 2019 derived a semi-empirical

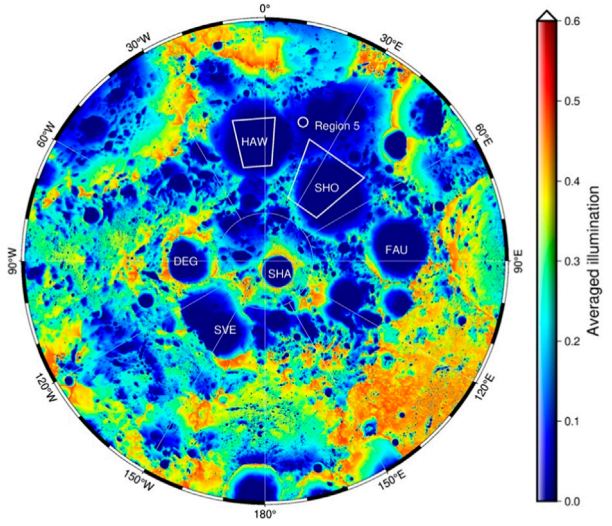

FIGURE 3
Annually averaged Sun illumination of the Moon's south pole (>85°S). The white trapezoids indicate study areas. HAW and SHO denote Haworth and Shoemaker, respectively. Other listed permanently shadowed craters are Shackleton (SHA), Faustini (FAU), De Gerlache (DEG), and Sverdrup (SVE). The white circle indicates "Region 5" which is supposed to have an upper limit heat flow value of 6 mW/m^2 (Paige and Siegler, 2016). The spatial resolution of the illumination map is 60 m/pixel, which is available at http://imbrium.mit.edu/.

model of C and K in the full range of 20–400 K by fitting lunar regolith simulant based on solid-state theory. Here, we adopt their model to calculate specific heat and thermal conductivity with the combination of Hayne et al.'s density model.

In order to solve the thermal model, we also need to input the surface temperature and interior heat flow. The thermal environment in polar regions is complex due to the complex illuminating conditions (Bussey et al., 2010; Mazarico et al., 2011; Gläser et al., 2014). Paige et al. (2010) modeled the Sun, the Earth, and the Moon as triangular meshes and used the ray tracing method to calculate lunar polar surface/subsurface temperatures at 500 m resolution. However, the simulation still presented about 15 K lower within PSRs than that of Diviner measurements during the daytime. The discrepancy is supposed to be caused by a directionally anisotropic thermal emission (Paige et al., 2010). In this study, we use diurnal variations of T_{bol} as input to constrain surface temperature instead of theoretical calculating to derive the subsurface temperatures (Wei et al., 2019; Schorghofer and Williams, 2020).

2.4 Scheme of heat flow inversion

The upper limit heat flow at "Region 5," an unnamed 3 km diameter and extremely cold crater (87.0°S, 15.3°E) which is located to the east of Haworth crater (see Figure 3) was retrieved from Diviner data (Paige and Siegler, 2016). In order to calculate the heat flow-dependent (lower boundary of Eq. 1) subsurface temperature with an unknown heat flow value, we set the upper limit heat flow as 24 mW/m^2 based on the maximum value of Apollo 15 HFE instead of Region 5's 6 mW/m^2. Thus, the heat flow can be inverted in the following steps. 1) Computing annual averaged (southern winter) subsurface temperatures with heat flows from 0 to 24 mW/m^2. 2) Modeling T_B based on the above temperature profiles (Wei et al., 2019; Feng et al., 2020; Siegler et al., 2020). 3) Match the modeled T_B and CE-2 observations and search for the best-fit heat flow value. Noting that although both the MRM observations and Diviner constrained simulations cover the same study area, they have different spatial resolutions and observation time ranges. Therefore, it could cause uncertainty by matching the modeled T_B and CE-2 observations directly. Here, we propose the following equation (Eq. 2) to minimize the discrepancy of T_B matching

$$r_{i,j} = \frac{c_i - c_j}{c_j}, \ (i = 1, j = 3, 4) \tag{2}$$

where the T_B-dependent ratio ($r_{i,j}$) is sensitive to heat flow because c_1 (3 GHz-channel) senses greater depths than the other two channels (19.35 and 37 GHz). Therefore, the heat flow can be inverted by comparing $r_{i,j}$ between MRM observations and modeled values. Figure 2 shows an example of the inversion scheme at Haworth and Shoemaker. It can be seen that the mean value of modeled $r_{1,4}$ (red lines) increases with heat flow at both craters gradually. The standard deviation of $r_{1,4}$ ratios (red shade) increase apparently with the increasing of heat flows, especially at Shoemaker. This is caused by the dominance of internal heat flow compared to the surface thermal state. The CE-2 data derived $r_{1,4}$ mean values (blue squares) then can be matched for searching the best heat flow values.

Note that the interior heat flow plays a part in near-surface temperature at PSRs and can be recorded by infrared measurements and microwave observations. However, compared to Diviner's infrared measurements at PSRs (Paige and Siegler, 2016), the longer wavelength of the microwave radiometer can sense greater depths for interior heat flow. Additionally, the discrepancy of spatial resolution between 3 GHz (25 km) and 19.35 GHz or 37 GHz (17.5 km) channels can be neglected because 1) the thermal environment including heat flow is supposed to be homogeneous for each MRM's field of view, and 2) the diurnal averaged T_B including all the data points covering the study area were derived for calculating $r_{1,3}$ and $r_{1,4}$ ratios.

3 Results

3.1 Lunar polar heat flow

To minimize the scattering effect, we select the data points near the bottom of each crater after filtering the southern winter data set. Figure 3 shows the modeled annually averaged Sun illumination of the lunar south polar region. The study area of the Haworth crater is 15–5°W, 87–88°S, and the Shoemaker's is 20–50°E, 87.3–88.6°S. It can be seen that the study areas enclosed by trapezoids at Haworth and Shoemaker present an extremely low illumination rate. Which indicates ideal places for heat flow inversion. The location of "Region 5" investigated by Paige and Siegler (2016) is also labeled in Figure 3 (white circle) which is near both of our study areas.

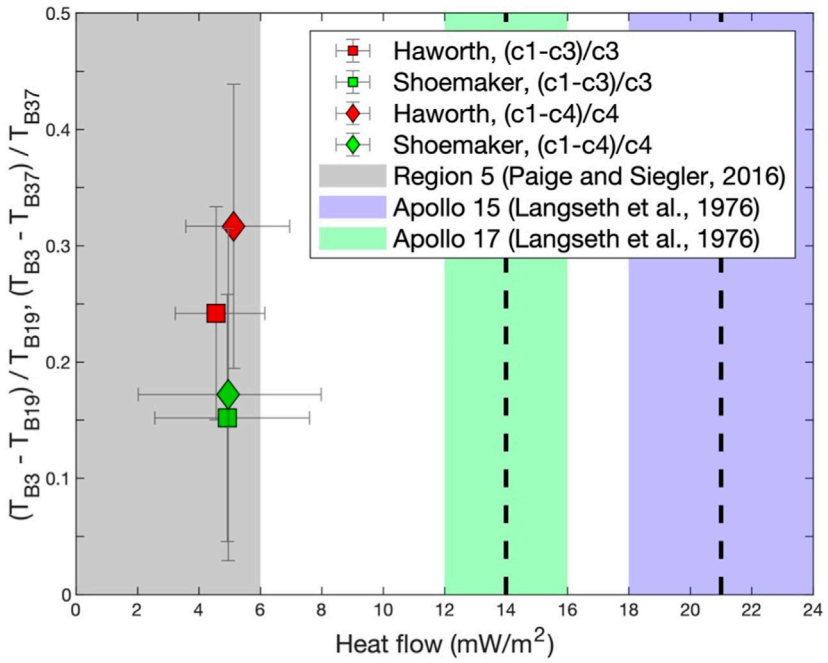

FIGURE 4
Retrieved heat flow at Haworth and Shoemaker. Other heat flow values at Region 5, Apollo 15, and 17 are presented in gray, green, and purple shades for comparison, respectively. The dashed line denotes the mean value. The vertical bar is the standard deviation of $r_{i,j}$, while the horizontal bar is the corresponding heat flow range.

Based on Eq. 2, ratios of $r_{1,3}$ and $r_{1,4}$ at study areas can be derived from observed (T_{B3}, T_{B19}) and (T_{B3}, T_{B37}), respectively. In addition, these ratios can also be derived from modeled T_B values, which are used for matching CE-2 observations (e.g., Figure 2). Figure 4 shows the retrieved heat flow at Haworth and Shoemaker using different T_B ratios. It can be seen that the averaged heat flows retrieved from $r_{1,3}$ and $r_{1,4}$ within the study area of Haworth crater (Figure 3, HAW) are ~4.6 and ~5.1 mW/m^2, respectively (Figure 4, red blocks). While the averaged heat flows within the study area of the Shoemaker crater (Figure 3, SHO) retrieved from $r_{1,3}$ and $r_{1,4}$ both are near to 4.9 mW/m^2 (Figure 4, green blocks). Note that each of the four values is averaged from thousands of data points covering the study areas based on different T_B ratios.

Although the two study areas present apparently different $r_{i,j}$ values, they have excellent consistency within their standard deviations (horizontal bars). It is worth noting that the uncertainty of inverted heat flow at the two craters varies from 1.3 to 3.0 mW/m^2 which is dependent upon the standard deviation of $r_{i,j}$. However, the good agreement of heat flow retrieved from different T_B ratios at each crater indicates the robustness of our inversion scheme. Furthermore, the averaged heat flow of the two craters is 4.9 ± 0.2 mW/m^2 which consists well with the upper limit of Region 5 (Figure 4 gray area), 6 mW/m^2 (Paige and Siegler, 2016). The similar heat flow in the two study areas suggests a relatively homogeneous interior thermal state of the Moon's south pole. Additionally, our retrieved heat flow is obviously less than that of Apollo 15 and 17 *in situ* measurements (Figure 4 green and purple shades) which are near the PKT unit.

Figure 5 shows the locations of Apollo 15 and 17 *in situ* heat flow experiments and our study areas on the Lunar Prospector gamma-ray spectrometer derived Th map (in a unit of ppm). The typical landing sites indicate that the measured heat flows might be greatly altered by deep subsurface radiogenic elements (Laneuville et al., 2013; Siegler and Smrekar, 2014) and lateral heat flow through highland/mare boundaries (Warren and Rasmussen, 1987). The study areas of PSRs are far from the PKT and highland/mare boundaries that will not enhance the sub-crust heat production and interior heat flow. In addition, the low content of surface Th at the south pole corresponds to low heat flow values while the larger Apollo 15 and 17 heat flow values correspond to highly concentrated Th. NASA's Gravity Recovery and Interior Laboratory observations show that the south pole has a roughly 40-km crustal thickness with feldspathic highland terrane associated with the low crustal thickness of the south pole Aitken basin (Wieczorek et al., 2013). The Urey ratio (the ratio between total internal heat production and total heat loss through the surface) assumed to be 0.5 is a good and representative of terrestrial planets and the Moon (Spohn and Breuer, 2002). Here, assuming the Th/U = 3.7 and K/U = 2,500 (Warren and Wasson, 1979), crustal density 2,550 kg/m^3 (Wieczorek et al., 2013), the Th bulk abundance of the lunar polar crust is constrained by 656 ± 54 ppb based on our retrieved mean heat flow (Haenel et al., 1988).

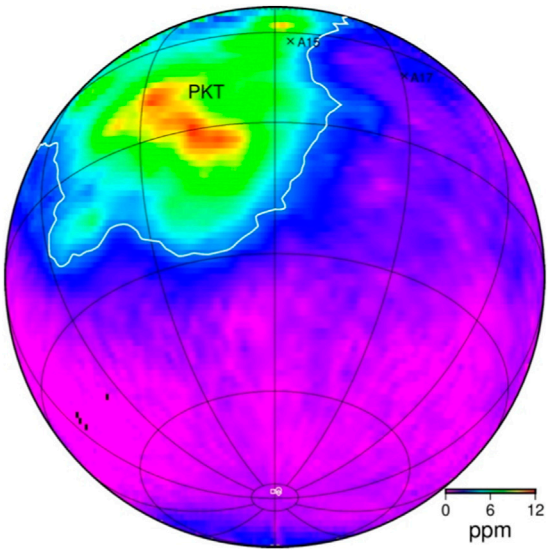

FIGURE 5
Locations of heat flow measurements on the Th map in a unit of ppm (Prettyman et al., 2006). The map is in orthographic projection centered at 0°E, 35°S. The crosses labeled A15 and A17 denote the Apollo 15 and 17 landing sites, respectively. The PKT area enclosed by the white line is constrained by the 3.5 ppm Th contour (Prettyman et al., 2006). The square, diamond, and circle denote the study areas of Haworth, Shoemaker, and Region 5 of the Moon's south pole, respectively.

3.2 Water ice effect on heat flow retrieval

Water ice is probably one of the most interesting and important elements in PSRs. The Lunar Crater Observation and Sensing Satellite (LCROSS) impact experiment confirmed that there is 5.6 ± 2.9wt% water ice at the impact site (Colaprete et al., 2010), and radar detections indicate that this water ice might present as small (<10 cm) and discrete pieces mixed with regolith rather than thick deposits of nearly pure water ice within a few meters of lunar surface (Neish et al., 2011). Furthermore, the regolith-ice mixture can behave differently with "dry" regolith in thermal emissions. Although water ice has been detected in PSRs and could be cold-trapped for billions of years (Siegler et al., 2016; Li et al., 2018), we still know less about the exact amount of water ice that appears in PSRs and the vertical distribution in the subsurface. This might lead to heat flow estimation uncertainty if water ice can influence the near-surface thermal regime obviously.

Assuming a mean regolith density of 1700 kg/m^3 with porosity 0.45 and ice density of 1,100 kg/m^3, the volumetric fraction of water ice (i.e., pore filling fraction, f_{ice}) at the LCROSS impact site is approximately 0.2. And the thermal property of ice-bearing regolith (TMP_{mix}) including density, thermal conductivity, and specific heat are calculated using the volumetric mixing model (Siegler et al., 2012), $TMP_{mix} = TMP_{reg} + p \cdot f_{ice} \cdot TMP_{ice}$, where p is the porosity of regolith which can be calculated from the bulk density of regolith, TMP_{reg} and TMP_{ice} are thermal property of regolith and ice, respectively. The dielectric constant of the mixture can be calculated based on a two-phase, three-dimensional medium mixing model at each layer (Bergman, 1978). To simplify the mixture thermal model, we suppose that water ice exists at the study area of Cabeus crater and diffuses homogeneously to different depths (z_{ice}) with the identical pore filling fraction (Figure 6).

Figure 7 shows the comparison of the T_{B3}/T_{B37} ratio between dry regolith (black line) and ice-bearing regolith with different diffusion depths (color-coded lines). It can be seen that the greater depths of water ice diffuse the less sensitive the T_{B3}/T_{B37} ratio is to the heat flow. This is mainly caused by increased lossy ice within 3 GHz sensed depths. For shallowly diffused depths, z_{ice} < 0.2 m, for example, the increasing of ice diffusion depth from 0.02 m (red line) to 0.2 m (green line) has relatively small influences in T_{B3}/T_{B37} ratio. However, it appears a large gap in the T_B ratio between the "dry" regolith and even small diffused ice within the top layer of 0.02 m. For greater diffusion depths, 0.5 (blue line) and 1 m (cyan line), for example, the T_{B3}/T_{B37} ratio presents a large discrepancy with respect to the "dry" regolith with increasing heat flow.

4 Discussion

4.1 Heat flow retrieved from icy regolith

Since it is unable to determine the exact amount of water ice that mixes with regolith and distributes in PSRs in what form, the *de facto* thermal emission might be more complex than we can model here. However, recent studies of near-infrared observations (Li et al., 2018) showed that only ~3.5% of cold traps of the south-polar region contained exposed water ice patches. It can be inferred that not the whole area of the study area can trap water ice and diffuse downward to a certain depth. A detailed water ice investigation in the future lunar mission such as China's unmanned Chang'E-7 lunar south polar exploration mission can help us to improve our thermal and microwave model, which could reveal more details of the subsurface thermal state.

Here, we use the scheme described in Section 2.4 to retrieve heat flow with scenarios of different ice diffusion depths that are discussed in Section 4.2. As shown in Table 1, compared to the "dry" regolith, the retrieved heat flow presents different ranges when ice diffused to the depth of 0.02, 0.2, 0.5, and 1 m at a constant pore filling fraction. The lower limit of heat flow (i.e., 0.6 mW/m^2) with different ice diffusion depths agrees well with the "dry" regolith except for the greater diffusion depth (z_{ice} = 1 m) which is 1.2 mW/m^2. The upper limit varies obviously (i.e., 5.9, 5.7, 3.3, 5.9 mW/m^2) with respect to "dry" regolith (4.6 mW/m^2) but is no more than 1.3 mW/m^2 in absolute difference. That is, water ice-bearing regolith has a small influence on heat flow inversion based on our ice diffusion model and retrieval scheme. It is worth noting that the retrieved heat flow values also have a good agreement with the upper limit of 6 mW/m^2 of Paige and Siegler (2016).

4.2 Rock effect

Radar observations at lunar polar regions suggested that the enhanced circular polarization ratio values might be caused by rocks rather than water ice deposits (Fa and Cai, 2013). Similar to the

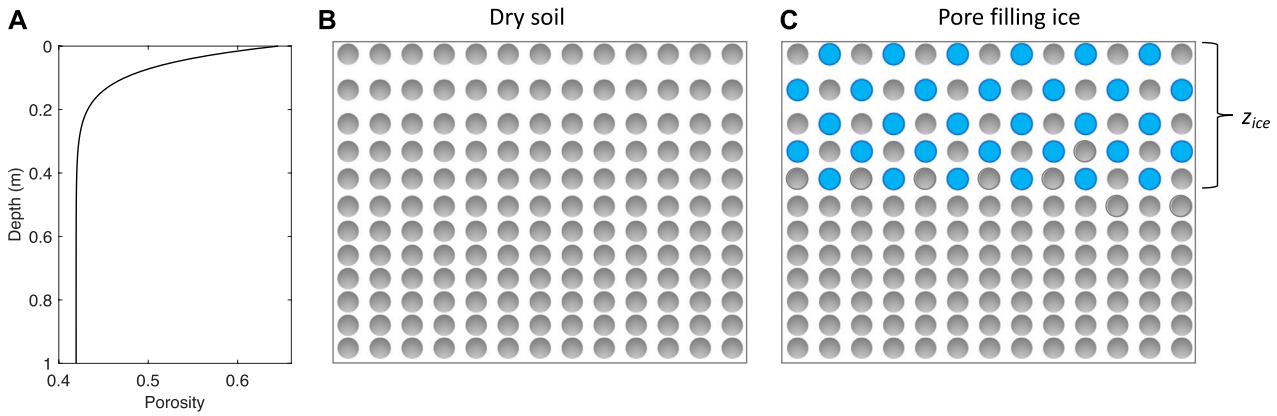

FIGURE 6
Profile of dry regolith porosity and ice-filling model. **(A)** is the porosity profile of dry lunar soil. **(B)** is the diagram of inhomogeneous dry soil from surface to a greater depth. **(C)** is the diagram with water ice that has been diffused to a certain depth of Z_{ice}.

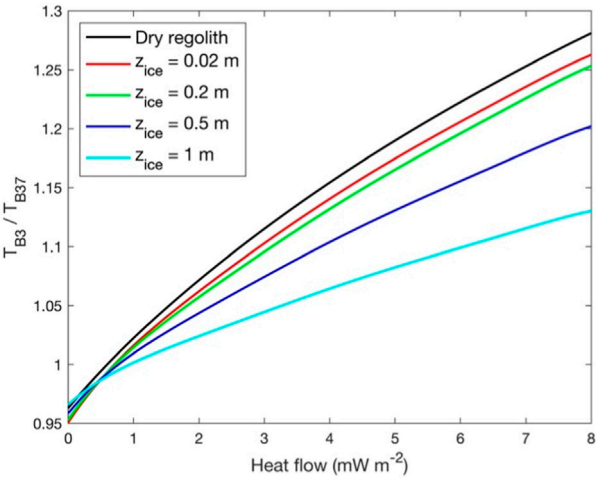

FIGURE 7
Variation of T_{B3}/T_{B37} ratio under different ice diffusion depths and interior heat flow at the Cabeus crater. The water ice pore filling fraction (f_{ice} = 0.2) is supposed to be homogeneously within each diffusion depth.

TABLE 1 Comparison of retrieved heat flows with different water ice diffusion depths at Cabeus crater. Water ice diffuses downward with a constant pore-filling fraction, f_{ice} = 0.2. Note that the cases of "dry" regolith and ice diffusion features correspond to Figure 7.

z_{ice} (m)	Dry regolith	0.02	0.2	0.5	1
HF (mW/m^2)	0.6–4.6	0.6–5.9	0.6–5.7	0.6–3.3	1.2–5.9

water ice effect, the perched and/or buried rocks can cause T_B anomaly due to their higher lossy property. The global average rock abundance (RA) within 60°N/S latitudes retrieved from Diviner measurements is 0.4% (Bandfield et al., 2011). The rock abundance referenced here is the area percentage within each pixel, and the diameter of the rock is larger than ~1 m. Since there is no quantity investigation of rock abundance at PSRs, we suppose that the polar region has a global averaged RA value. Following Bandfield et al.'s model that the regolith-rock mixture can be simplified as columns of regolith and rock within each pixel, we assume that both regolith and rocks observed by Diviner behave the same surface temperature within each bin (200 m × 200 m). Thus, we modeled the regolith-rock mixture T_B by weighting the RA value (0.4%) within each pixel. We found that the modeled $r_{i,j}$ varies slightly with heat flow 4.9 mW/m^2 compared to the rock-free (pure "dry" regolith) model, which suggests that the rock effect on heat flow inversion can be neglected based on our method.

4.3 Application for constraining water ice loss rate

Lunar polar volatiles, including water, are important for understanding the depletion, delivery, weathering, and orbital evolution of the Moon (Paige et al., 2010; Siegler et al., 2016). The water ice distribution is also crucial for *in situ* resource utilization of future lunar exploration (Cannon and Britt, 2020). Here, we discuss the thermal stability of water ice in polar regions which is controlled by the near-surface thermal environment rather than the accumulation from water-bearing meteoroids and/or the punctuation by impacts (Cannon et al., 2020). Note that the southern summer Diviner data are used here to calculate the maximum subsurface temperature and constrain the maximum sublimation rate of water ice. Neglecting the influence of water ice in regolith thermal property, we can derive subsurface temperatures using Diviner measurements and our retrieved heat flow as boundary inputs (Eq. 1). Following the work of Paige et al. (2010), Schorghofer and Taylor (2007), we calculate the loss rate of water ice at different depths and search a certain depth at which the sublimation rate equals 1 kg/(m^2 · Ga) at the lunar south pole.

Figure 8 shows the distribution of water ice at different depths with a constant sublimation rate. It can be seen apparently that water ice distributes from small to large depressions/craters. And most water ice is cold trapped in shallow depths (<10 cm) or even exposes

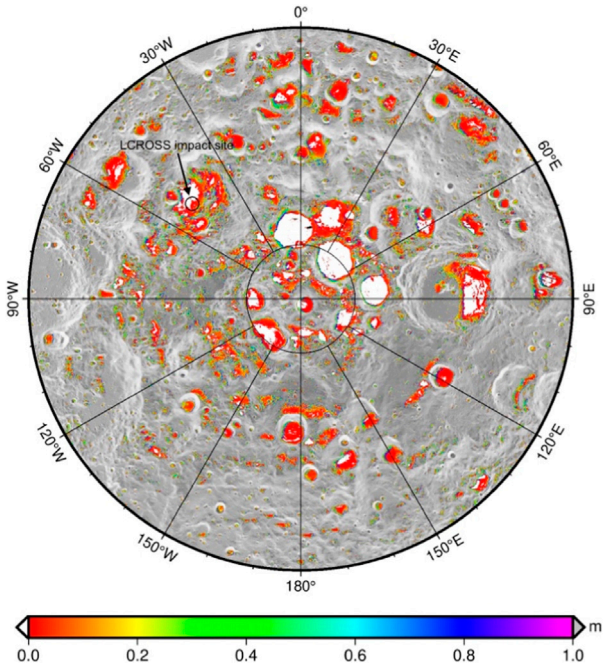

FIGURE 8
Diffusion depths of water ice with sublimation rate 1 kg/(m^2 · Ga) which is constrained by Diviner measurements and our retrieved heat flow at the lunar south polar region. The white color indicates that water ice is exposed on the surface, while the gray region indicates that the water ice can be cold trapped in a depth greater than 1 m. The circle indicates the LCROSS impact site. The outmost circle is 80°S latitude.

on the surface, for example, the LCROSS impact site (Figure 8 black circle). Compared to Paige et al.'s model which has not considered specific constraints from seasonal variation of surface T_{bol} and retrieved interior heat flow, our result provides an additional thermal constraint for the thermal stability of water ice at cold traps. For example, our model suggests that the partially sunlit Amundsen crater floor (84.5°S, 82.8°E) may harbor water ice with a loss rate of 1 mm/Ga at greater depths (>1 m) while Paige et al.'s model indicates <0.5 m depth. Thus, accurate constraints of subsurface temperatures can help us to evaluate water ice thermal stability, which is significant for investigating the depletion history of volatiles and even landing site selection for mining water ice in the future lunar exploration (Cannon and Britt, 2020).

5 Conclusion

In this study, we retrieved interior heat flow at Haworth and Shoemaker from ~10 years of Diviner measurements and CE-2 observations. The retrieved heat flows at the two craters have excellent consistency, which also agrees well with Diviner-derived Region 5 (Paige and Siegler, 2016). The average value is 4.9 ± 0.2 mW/m^2 which suggests a homogeneous interior heat flux. Assuming a uniform heat flow at the lunar south pole, the bulk content of Th of the lunar polar crust is constrained by 656 ± 54 ppb based on the Urey ratio of the Moon. In addition, we also estimated the thermal stability of water ice which is constrained by Diviner observations and retrieved heat flow. We found that water ice with a constant loss rate of 1 kg/(m^2·Ga) can be cold-trapped from the surface to shallow depths (<0.1 m) within most parts of the PSRs of the Moon. Finally, our study provides a new method to constrain the lunar subsurface thermal state at the non-PKT area by reconciling the unprecedented MRM data and longevous Diviner observations. The retrieved heat flow helps us to understand the subsurface thermal state and thermal history of the Moon.

Data availability statement

The Diviner Tbol data set was obtained from the NASA Planetary Data System Geosciences Node, available at http://pds-geosciences.wustl.edu/missions/lro/diviner.htm. CE-2 Microwave Radiometer data were provided by the Ground Research and Application System of the Chinese Lunar Exploration Program and can be downloaded from https://doi.org/10.5281/zenodo.5164204.

Author contributions

GW conceptualized this study and processed the data. XL, HG, and YS provided data interpretations. GW prepared figures and tables and wrote the draft. HG discussed the results and revised the manuscript. All authors contributed to the article and approved the submitted version.

Funding

GW was supported by the National Key Research and Development Program of China (2022YFF0711400), the B-type Strategic Priority Program of the Chinese Academy of Sciences (XDB 41000000), the National Natural Science Foundation of China (42241154), and Science and Technology Program of Guizhou Province [QKHJC-ZK(2023)-476]. HG was supported by the National Natural Science Foundation of China (41903058), Frontier Science Research Program of Deep Space Exploration Laboratory (2022-QYKYJH-HXYF023), and Science and Technology Program of Guizhou Province [QKHJC-ZK(2023)-131].

Acknowledgments

We thank Stephen J. Keihm for his constructive comments and discussion of the early version of the manuscript. We also thank Jean-Pierre Williams for the helpful discussion about using Diviner T_{bol} data.

Conflict of interest

The authors declare that the research was conducted in the absence of any commercial or financial relationships that could be construed as a potential conflict of interest.

Publisher's note

References

Bandfield, J. L., Ghent, R. R., Vasavada, A. R., Paige, D. A., Lawrence, S. J., and Robinson, M. S. (2011). Lunar surface rock abundance and regolith fines temperatures derived from LRO Diviner Radiometer data. *J. Geophys. Res.* 116, E00H02. doi:10.1029/2011JE003866

Bergman, D. J. (1978). The dielectric constant of a composite material—a problem in classical physics. *Phys. Rep.* 43, 377–407. doi:10.1016/0370-1573(78)90009-1

Bussey, D. B. J., McGovern, J. A., Spudis, P. D., Neish, C. D., Noda, H., Ishihara, Y., et al. (2010). Illumination conditions of the south pole of the Moon derived using Kaguya topography. *Icarus* 208, 558–564. doi:10.1016/j.icarus.2010.03.028

Cannon, K. M., and Britt, D. T. (2020). A geologic model for lunar ice deposits at mining scales. *Icarus* 347, 113778. doi:10.1016/j.icarus.2020.113778

Cannon, K. M., Deutsch, A. N., Head, J. W., and Britt, D. T. (2020). Stratigraphy of ice and ejecta deposits at the lunar Poles. *Geophys. Res. Lett.* 47. doi:10.1029/2020GL088920

Colaprete, A., Schultz, P., Heldmann, J., Wooden, D., Shirley, M., Ennico, K., et al. (2010). Detection of water in the LCROSS ejecta plume. *Science* 330, 463–468. doi:10.1126/science.1186986

De Rosa, D., Bussey, B., Cahill, J. T., Lutz, T., Crawford, I. A., Hackwill, T., et al. (2012). Characterisation of potential landing sites for the European Space Agency's Lunar Lander project. *Planet. Space Sci.* 74, 224–246. doi:10.1016/j.pss.2012.08.002

Elder, C. M., Douglass, B., Ghent, R. R., Hayne, P. O., Williams, J. -P., Bandfield, J. L., et al. (2019). The subsurface coherent rock content of the moon as revealed by cold-spot craters. *J. Geophys. Res. Planets* 124, 3373–3384. doi:10.1029/2019JE006128

Fa, W., and Cai, Y. (2013). Circular polarization ratio characteristics of impact craters from mini-RF observations and implications for ice detection at the polar regions of the moon: Lunar cpr properties for ice detection. *J. Geophys. Res. Planets* 118, 1582–1608. doi:10.1002/jgre.20110

Feng, J., Siegler, M. A., and Hayne, P. O. (2020). New constraints on thermal and dielectric properties of lunar regolith from LRO diviner and CE-2 microwave radiometer. *J. Geophys. Res. Planets* 125. doi:10.1029/2019JE006130

Gläser, P., Scholten, F., De Rosa, D., Marco Figuera, R., Oberst, J., Mazarico, E., et al. (2014). Illumination conditions at the lunar south pole using high resolution Digital Terrain Models from LOLA. *Icarus* 243, 78–90. doi:10.1016/j.icarus.2014.08.013

Grott, M., Knollenberg, J., and Krause, C. (2010). Apollo lunar heat flow experiment revisited: A critical reassessment of the *in situ* thermal conductivity determination. *J. Geophys. Res.* 115, E11005. doi:10.1029/2010JE003612

Haenel, R., Rybach, L., and Stegena, L. (1988). *Handbook of terrestrial heat-flow density determination*. Springer.Berlin, Germany.

Hagermann, A., and Tanaka, S. (2006). Ejecta deposit thickness, heat flow, and a critical ambiguity on the Moon. *Geophys. Res. Lett.* 33, L19203. doi:10.1029/2006GL027030

Hayne, P. O., Bandfield, J. L., Siegler, M. A., Vasavada, A. R., Ghent, R. R., Williams, J.-P., et al. (2017). Global regolith thermophysical properties of the moon from the diviner lunar radiometer experiment: Lunar regolith thermophysical properties. *J. Geophys. Res. Planets* 122, 2371–2400. doi:10.1002/2017JE005387

Jolliff, B. L., Gillis, J. J., Haskin, L. A., Korotev, R. L., and Wieczorek, M. A. (2000). Major lunar crustal terranes: Surface expressions and crust-mantle origins. *J. Geophys. Res.* 105, 4197–4216. doi:10.1029/1999JE001103

Keihm, S. J. (1984). Interpretation of the lunar microwave brightness temperature spectrum: Feasibility of orbital heat flow mapping. *Icarus* 60, 568–589. doi:10.1016/0019-1035(84)90165-9

Keihm, S. J., and Langseth, M. G. (1975). Lunar microwave brightness temperature observations reevaluated in the light of Apollo program findings. *Icarus* 24, 211–230. doi:10.1016/0019-1035(75)90100-1

Kiefer, W. S. (2012). Lunar heat flow experiments: Science objectives and a strategy for minimizing the effects of lander-induced perturbations. *Planet. Space Sci.* 60, 155–165. doi:10.1016/j.pss.2011.07.016

Laneuville, M., Wieczorek, M. A., Breuer, D., and Tosi, N. (2013). Asymmetric thermal evolution of the moon: Lunar evolution. *J. Geophys. Res. Planets* 118, 1435–1452. doi:10.1002/jgre.20103

Langseth, M. G., Keihm, S. J., and Peters, K. (1976). Revised lunar heat-flow values. *Present. A. T. Proc. Lunar Sci. Conf.* 7th, 3143–3171.

Li, S., Lucey, P. G., Milliken, R. E., Hayne, P. O., Fisher, E., Williams, J.-P., et al. (2018). Direct evidence of surface exposed water ice in the lunar polar regions. *Proc. Natl. Acad. Sci. U. S. A.* 115, 8907–8912. doi:10.1073/pnas.1802345115

Mazarico, E., Neumann, G. A., Smith, D. E., Zuber, M. T., and Torrence, M. H. (2011). Illumination conditions of the lunar polar regions using LOLA topography. *Icarus* 211, 1066–1081. doi:10.1016/j.icarus.2010.10.030

Meng, Z., Chen, S., Osei, E. M., Wang, Z., and Cui, T. (2010). Research on water ice content in Cabeus crater using the data from the microwave radiometer onboard Chang'e-1 satellite. *Sci. China Phys. Mech. Astron.* 53, 2172–2178. doi:10.1007/s11433-010-4159-y

Nagihara, S., Kiefer, W. S., Taylor, P. T., Williams, D. R., and Nakamura, Y. (2018). Examination of the long-term subsurface warming observed at the Apollo 15 and 17 sites utilizing the newly restored heat flow experiment data from 1975 to 1977. *J. Geophys. Res. Planets* 123, 1125–1139. doi:10.1029/2018JE005579

Neish, C. D., Bussey, D. B. J., Spudis, P., Marshall, W., Thomson, B. J., Patterson, G. W., et al. (2011). The nature of lunar volatiles as revealed by Mini-RF observations of the LCROSS impact site. *J. Geophys. Res.* 116, E01005. doi:10.1029/2010JE003647

Paige, D. A., and Siegler, M. A. 2016"New constraints on lunar heat flow rates from LRO diviner lunar radiometer experiment polar observations," in Proceedings of the 47th Lunar and Planetary Science Conference. Presented at the 47th Lunar and Planetary Science Conference, Houston, TX, USA, January 2016, 2753.

Paige, D. A., Siegler, M. A., Zhang, J. A., Hayne, P. O., Foote, E. J., Bennett, K. A., et al. (2010). Diviner lunar radiometer observations of cold traps in the moon's south polar region. *Science* 330, 479–482. doi:10.1126/science.1187726

Prettyman, T. H., Hagerty, J. J., Elphic, R. C., Feldman, W. C., Lawrence, D. J., McKinney, G. W., et al. (2006). Elemental composition of the lunar surface: Analysis of gamma ray spectroscopy data from lunar prospector: Lunar elemental composition. *J. Geophys. Res.* 111.2656 doi:10.1029/2005je002656

Qiao, L., Head, J. W., Wilson, L., and Ling, Z. (2021). Ina lunar irregular mare patch mission concepts: Distinguishing between ancient and modern volcanism models. *Planet. Sci. J.* 2, 66. doi:10.3847/PSJ/abeaa0

Saito, Y. 2008"The long term temperature variation in the lunar subsurface," in Proceedings of the Presented at the Lunar and Planetary Science Conference 39th (2008), Houston, TX, USA, March 2008, 1663.

Schloerb, F. P., Muhleman, D. O., and Berge, G. L. (1976). Lunar heat flow and regolith structure inferred from interferometric observations at a wavelength of 49.3 cm. *Icarus* 29, 329–341. doi:10.1016/0019-1035(76)90137-8

Schorghofer, N., and Taylor, G. J. (2007). Subsurface migration of H_2O at lunar cold traps. *J. Geophys. Res.* 112, E02010. doi:10.1029/2006JE002779

Schorghofer, N., and Williams, J.-P. (2020). Mapping of ice storage processes on the moon with time-dependent temperatures. *Planet. Sci. J.* 1, 54. doi:10.3847/PSJ/abb6ff

Siegler, M. A., Feng, J., Lucey, P. G., Ghent, R. R., Hayne, P. O., and White, M. N. (2020). Lunar titanium and frequency-dependent microwave loss tangent as constrained by the Chang'E-2 MRM and LRO diviner lunar radiometers. *J. Geophys. Res. Planets* 125. doi:10.1029/2020JE006405

Siegler, M., Aharonson, O., Carey, E., Choukroun, M., Hudson, T., Schorghofer, N., et al. (2012). Measurements of thermal properties of icy mars regolith analogs: Thermal properties OF ICY mars regolith. *J. Geophys. Res.* 117. doi:10.1029/2011je003938

Siegler, M. A., Miller, R. S., Keane, J. T., Laneuville, M., Paige, D. A., Matsuyama, I., et al. (2016). Lunar true polar wander inferred from polar hydrogen. *Nature* 531, 480–484. doi:10.1038/nature17166

Siegler, M. A., and Smrekar, S. E. (2014). Lunar heat flow: Regional prospective of the Apollo landing sites: Regional lunar heat flow. *J. Geophys. Res. Planets* 119, 47–63. doi:10.1002/2013JE004453

Spohn, T., and Breuer, D. 2002"Surface heat flow, radiogenic heating, and the evolution of the moon," in Proceedings of the EGS 27th General Assembly, Nice, France, April 2002, 6000.

Vasavada, A. (1999). Near-surface temperatures on mercury and the moon and the stability of polar ice deposits. *Icarus* 141, 179–193. doi:10.1006/icar.1999.6175

Vasavada, A. R., Bandfield, J. L., Greenhagen, B. T., Hayne, P. O., Siegler, M. A., Williams, J.-P., et al. (2012). Lunar equatorial surface temperatures and regolith properties from the diviner lunar radiometer experiment: Lunar equatorial regolith properties. *J. Geophys. Res.* 117.3987 doi:10.1029/2011JE003987

Warren, P. H., and Rasmussen, K. L. (1987). Megaregolith insulation, internal temperatures, and bulk uranium content of the moon. *J. Geophys. Res.* 92, 3453. doi:10.1029/JB092iB05p03453

Warren, P. H., and Wasson, J. T. (1979). The origin of KREEP. *Rev. Geophys.* 17, 73. doi:10.1029/RG017i001p00073

Wei, G., Li, X., Gan, H., Blewett, D. T., Neish, C. D., and Greenhagen, B. T. (2019). A new method for simulation of lunar microwave brightness temperatures and evaluation of Chang'E-2 MRM data using thermal constraints from diviner. *J. Geophys. Res. Planets*.29 5858, doi:10.1029/2018JE005858

Wei, G., Li, X., Zhang, W., Tian, Y., Jiang, S., Wang, C., et al. (2023). Illumination conditions near the Moon's south pole: Implication for a concept design of China's Chang'E−7 lunar polar exploration. *Acta Astronaut.* 208, 74–81. doi:10.1016/j.actaastro.2023.03.022

Wieczorek, M. A., Neumann, G. A., Nimmo, F., Kiefer, W. S., Taylor, G. J., Melosh, H. J., et al. (2013). The crust of the moon as seen by GRAIL. *Science* 339, 671–675. doi:10.1126/science.1231530

Wieczorek, M. A., and Phillips, R. J. (2000). The "Procellarum KREEP Terrane": Implications for mare volcanism and lunar evolution. *J. Geophys. Res.* 105, 20417–20430. doi:10.1029/1999JE001092

Williams, J. -P., Greenhagen, B. T., Paige, D. A., Schorghofer, N., Sefton-Nash, E., Hayne, P. O., et al. (2019). Seasonal polar temperatures on the moon. *J. Geophys. Res. Planets* 124, 2505–2521. doi:10.1029/2019JE006028

Woods-Robinson, R., Siegler, M. A., and Paige, D. A. (2019). A model for the thermophysical properties of lunar regolith at low temperatures. *J. Geophys. Res. Planets* 124, 1989–2011. doi:10.1029/2019JE005955

Zheng, Y.-C., Chan, K. L., Tsang, K. T., Zhu, Y.-C., Hu, G. P., Blewett, D. T., et al. (2019). Analysis of Chang'E-2 brightness temperature data and production of high spatial resolution microwave maps of the Moon. *Icarus* 319, 627–644. doi:10.1016/j.icarus.2018.09.036